CHEMISTRY OF MATERIALS

pubs.acs.org/cm Article

Computational Prediction of Boron-Based MAX Phases and MXene Derivatives

Nanxi Miao, Junjie Wang,* Yutong Gong, Jiazhen Wu, Haiyang Niu, Shiyao Wang, Kun Li, Artem R. Oganov,* Tomofumi Tada, and Hideo Hosono

Cite This: *Chem. Mater.* 2020, 32, 6947−6957 Read Online

ACCESS | Metrics & More | Article Recommendations | Supporting Information

ABSTRACT: Conventional MAX phases (M is an early transition metal, A represents a p-block element or Cd, and X is carbon or nitrogen) have so far been limited to carbides and/or nitrides. In the present work, a series of stable layered ternary borides were predicted by combining variable-composition evolutionary structure search and first-principles calculations. The predicted Hf_2InB_2, Hf_2SnB_2, Zr_2TlB_2, Zr_2PbB_2, and Zr_2InB_2 show a Ti_2InB_2 type of structure (space group $P\bar{6}m2$, No. 187, *Nat. Commun.* 2019, 10, 2284), and the structures of Hf_3PB_4 and Zr_3CdB_4 share the same space group with Ti_2InB_2 but belong to a new structure type. These two structural prototypes, M_2AB_2 and M_3AB_4 (M is Zr or Hf), have the composition and local structures of MAB phases, but inherit a hexagonal symmetry of MAX phases. Moreover, Hf_2BiB and Hf_2PbB exhibit a typical structure of conventional MAX phases ($M_{n+1}AX_n$, space group $P6_3/mmc$, No. 194). These findings suggest that boron-based ternary compounds may be a new platform of MAX phases. The functionalized two-dimensional (2D) borides derived from the predicted ternary phases are calculated to be with improved mechanical flexibility and adjustable electronic properties relative to the parent ones. In particular, the 2D $Hf_2B_2T_2$ and $Zr_2B_2T_2$ (T = F, Cl) can transform from metal to semiconductor or semimetal under appropriate compressive biaxial strains. Moreover, the 2D Zr_2B_2 exhibits a high theoretical lithium-ion (Li^+) storage capacity and low Li^+ migration energy barriers. These novel properties render 2D boron-based materials promising candidates for applications in flexible electronic devices and Li^+ battery anode materials.

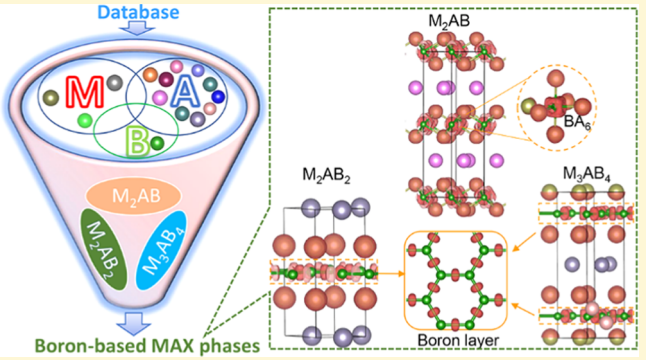

INTRODUCTION

Conventional MAX phases have been detailed as two-dimensional (2D) $M_{n+1}X_n$ sublattices interleaved by A layers, where M is an early transition metal, A represents a p-block element or Cd, and X has so far been limited to carbon and/or nitrogen.[1] The M−X bond is usually much stronger than the M−A metallic bond, which makes it possible to remove "A" layers from the bulk.[2−4] The synthesis of 2D titanium carbide (Ti_3C_2) by selective etching of aluminum (Al) from the MAX phase Ti_3AlC_2 in 2011 has led to the discovery of a new family of 2D transition-metal carbides/nitrides, which were named as MXenes.[5] With high specific surface area, superior mechanical strength, excellent electrical conductivity, tunable surface terminations, and the ability to accommodate intercalants, MXenes are promising for broad application areas including energy storage,[6−18] catalysis,[19,20] electromagnetic wave absorption and interference shielding,[21−23] etc.

Motivated by the potential applications of MXenes, searching for new layered compounds has drawn considerable attention in the past years.[24−34] One simple attempt can be done by replacing C/N atoms with boron; however, such a strategy has not been successful so far.[35] From the nature of anisotropic chemical bonding, it is expected that the thermodynamic stability of MAX phases can be majorly determined by the M−X bonding of $M_{n+1}X_n$ layer, i.e., the stability of M−X octahedra shown in Figure 1a. Since the electronegativity (Allen scale)[36−38] of boron atom (2.05 eV) is much smaller than that of the C (2.54 eV) or N (3.07 eV) atom, the charge transfer between M and boron atoms in the $M_{n+1}B_n$ layer is much weaker than that in the conventional $M_{n+1}X_n$ layer. Consequently, it is expected that the M−B bond is weaker than M−C or M−N, implying lower thermodynamic stability of boron-containing MAX phase compared to that of the carbide or nitride counterparts.

In 2015, a new family of layered transition-metal borides named MAB phases (M, A, and B represent an early transition metal, IIIA or IVA group element, and boron, respectively) was

Received: May 22, 2020
Revised: July 22, 2020
Published: July 22, 2020

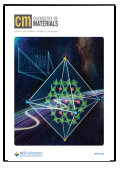

https://dx.doi.org/10.1021/acs.chemmater.0c02139
Chem. Mater. 2020, 32, 6947−6957

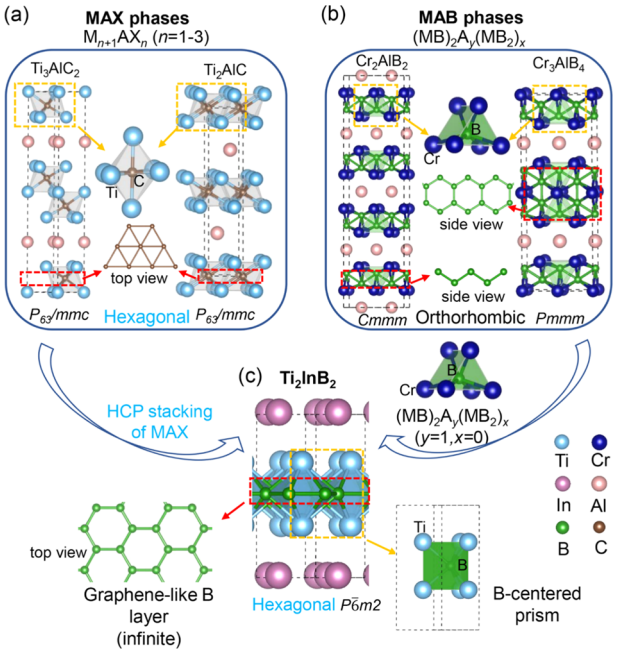

Figure 1. Crystal structures and compositions of MAX phases and MAB phases. (a) Representative conventional MAX phases Ti_2AlC and Ti_3AlC_2; Ti (M), Al (A), and C(X) atoms alternately stack along a hexagonal close-packed (HCP) style and form atomic layers that are parallel to each other; $M_{n+1}X_n$ layers can change from M_2X to M_4X_3, and in each stabilization unit, $M_{n+1}X_n$, all X atoms fill the octahedral interstitial of M atoms (illustrated with orange frames) and the X atoms form a triangle X−X grid (illustrated with red frames). (b) Typical MAB phases Cr_3AlB_4 and Cr_2AlB_2; boron atoms and metal atoms in the MAB phases form trigonal prisms BM_6 (labeled with orange frame); zigzag B chains or chains of edge-sharing B-hexagons are formed by sharing rectangular faces of B-centered prisms (illustrated with red frames). (c) Newly discovered ternary boride Ti_2InB_2,[24] which inherit the HCP stacking of MAX phases as well as local structure and composition of MAB phases.

proposed by Ade and Hillebrecht.[39] Recently, Kota et al. reviewed the synthetic methods, crystal structure, chemical bonding, and characteristic properties of MAB phases.[40] Several experimental and theoretical results demonstrate that MAB phases could be exfoliated into 2D transition-metal borides (MBenes).[41−43] MBenes are expected to have potential application in energy storage,[43,44] catalysis,[45] magnetic materials,[46] etc. Different from MAX phases, the composition of MAB phases can be described as $(MB)_2A_y(MB_2)_x$, where the boride layers are separated by a single layer or double layers of A atoms. As shown in Figure 1b, MAB phases reveal a crystal structure of orthorhombic space group and boron atoms sit at the centers of M prisms. In addition, both strong M−B bonding and covalent B−B bonding constitute the layered structures and make MAB phases significantly stable. The structural characteristics of the discovered MAB phases encouraged us to design boron-containing MAX phases based on an idea that the thermodynamic stability can be robustly improved via introducing boron−boron bonding by increasing boron concentration.

In a very recent work, a hexagonal layered ternary boride Ti_2InB_2 was first predicted and then experimentally synthesized by Wang et al.[24] As shown in Figure 1c, the crystal structure of Ti_2InB_2 exhibits typical characteristics of MAX phases: two M (Ti) layers and one A (In) layer are closely packed in an HCP A−B−A sequence, forming a layered structure. The space group of the Ti_2InB_2 structure was identified as $P\bar{6}m2$ (No. 187), which is a hexagonal subgroup of the space group for conventional MAX phases (space group $P6_3/mmc$, No. 194). However, the composition of Ti_2InB_2 is analogous to the formula $(MB)_2A_y(MB_2)_x$ of MAB phases (e.g., Cr_2AlB_2) and is different from that ($M_{n+1}AX_n$) of MAX phases. Boron atoms in Ti_2InB_2 occupy the X sites between double M layers and form a graphene-like layer with strong covalent B−B bonding rather than a triangle (close-packed) layer (Figure 1c) because the B/Ti ratio (1.0) is higher than those X/M ratios ($n/(n + 1)$) in conventional MAX phases. The discovery of Ti_2InB_2 can be regarded as an extension of the concept of conventional MAX phases and confirms our idea that the boron−boron bonding can improve the stability of boride MAX phases. However, this study also raises interesting questions of whether boride MAX phases are as rich a class of phases as traditional MAX phases and whether the conventional composition of $M_{n+1}AX_n$ can be realized in the boride phases.

As M−X bonds have a significant ionic component, the stability of the compound is closely related to the electronegativity difference between M and X atoms, say, the polarity of M−X bonds.[47] Therefore, a possible way to improve the stability of the BM_6 octahedron can be enhancing the charge transfer from M to B via choosing a proper transition metal M, which exhibits lower electronegativity than Ti. In the periodic table of elements, only Zr (1.32 eV) or Hf (1.16 eV) has a lower electronegativity than Ti (1.38 eV) among IVB group transition metals,[36−38] which is possible to form a stronger M−B bond than Ti−B. Here, we present a systematic high-throughput structure search using Ti, Zr, and Hf as M components, predicting a series of stable ternary borides with the typical features of MAX phases. Three types of new layered borides were obtained from this study, including M_2AB, M_2AB_2, and M_3AB_4. More interestingly, the predicted borides Hf_2BiB and Hf_2PbB show identical structural features with the traditional M_2AX phases. The dynamic and thermal stabilities of all predicted compounds were carefully checked. The separation energy calculations suggest that the newly predicted MAX phases may be exfoliated into MXenes by selective etching of A layers. The effects of different terminated functional groups and biaxial strains on the electronic structures and mechanical properties of the new MXenes were also examined. Finally, we predict that 2D Zr_2B_2 is promising as an anode material in Li-ion battery.

COMPUTATIONAL DETAILS

Structure searches for stable ternary borides were carried out within the computational framework illustrated in Figure 2. The stable phases in the M−A−B systems were searched using most p-block elements and Cd as the A component. To accelerate the structure search, a dataset for the prototypes of available MAX phases was constructed and used as seed structures for different systems. The initialized dataset includes prototypes "312" (e.g., Ti_3AlC_2), "211" (e.g., Ti_2AlC), and "212" (Ti_2InB_2). For each ternary system, preliminary pseudo-binary variable-composition searches[48,49] were conducted to estimate the thermodynamic stability of ternary borides with respect to assumed binary borides M_xB_z and A metals. Stable binary-component M_xB_z and A metals were used as ending components in a pseudo-binary variable-composition search, which means any ratios of M_xB_z to A were considered to construct ternary structures, with the limitation of the total number of atoms being ≤40. The stable ternary borides suggested by the preliminary search were then

https://dx.doi.org/10.1021/acs.chemmater.0c02139
Chem. Mater. 2020, 32, 6947−6957

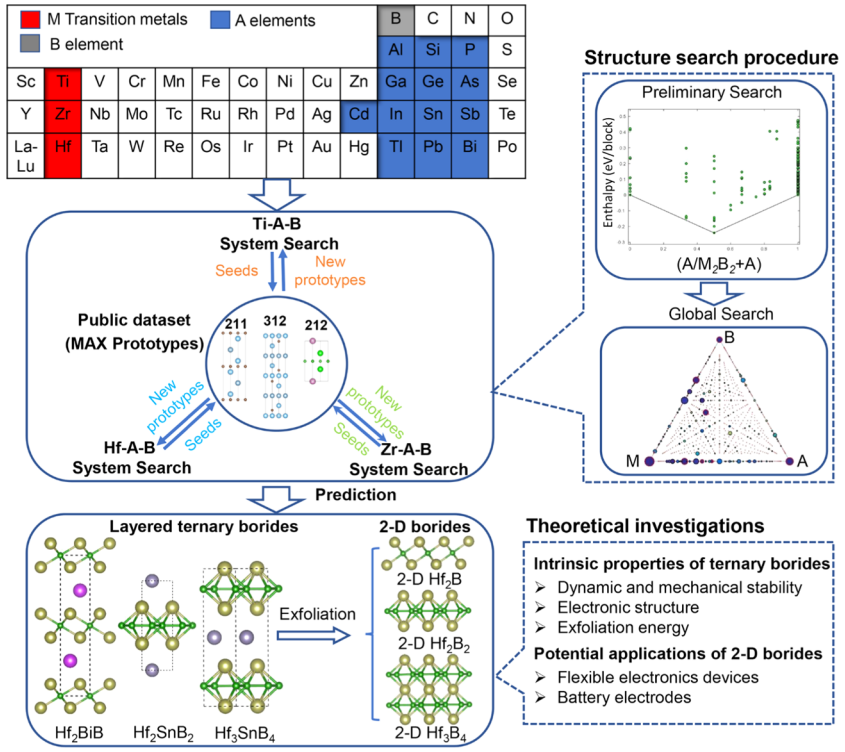

Figure 2. Computational approach for the discovery of ternary borides. Each ternary compound structure search consists of a pseudo-binary structure search (preliminary search) and a ternary structure search (global search). Theoretical investigations were performed for each predicted layered ternary compound and its derived 2D structures.

input to a ternary variable-composition search to evaluate its global stability by considering all possible competing phases in Materials Project database,[50] as shown in Figure 2. All structure searches were performed through a combination of Universal Structure Predictor: Evolutionary Xtallography (USPEX)[51−53] and the Vienna Ab initio Simulation Package (VASP).[54] All possible combinations of M elements (Ti, Zr, and Hf), A elements (p-block metals and Cd, as illustrated in Figure 2), and boron were considered within the limitation of 40 atoms in the primitive cell. As shown in Figure 2, the new prototypes found in the global structure search of certain ternary system would be put into the public dataset and be used to speed up other searches. For example, the metastable structure Ti_3InB_4 preferentially screened in the Ti−A−B, which can be used as a seed structure to participate in the screening of the Hf−A−B system, thereby improving the screening efficiency.

In VASP calculations, the projector augmented wave potential (PAW)[55] method was used with a plane-wave cutoff energy of 600 eV. The version of PAW potentials used in our work is potpaw_PBE.54 (Table S1, Supporting Information). The electronic exchange-correlation interactions were described by the generalized gradient approximation (GGA) in the Perdew−Burke−Ernzerhof (PBE) formulation.[56] In the Brillouin zone, a dense *k*-point grid with the resolution $2\pi \times 0.04$ Å^{-1} was used for high-throughput structure searches, and $2\pi \times 0.02$ Å^{-1} was used for the structure optimizations and electronic structure calculation. All stable structures were optimized with force convergence during the relaxation to 10^{-3} eV/Å. The dynamic stability of thermodynamically stable structures was checked through phonon dispersion calculations using density functional perturbation theory (DFPT), as implemented in the Phonopy program.[57] Ab initio molecular dynamics (AIMD)[58] simulations were performed to explore the thermal stability of MAX phases and the derived MXenes. For the 2D borides calculations, a large vacuum space of 40 Å was set to avoid any interactions between two neighboring monolayers along the *c* axis due to periodic boundary conditions. A 3 × 3 × 1 supercell was adapted for the 2D structures in the AIMD simulation. Strains were imposed by compressing/stretching the lattice in the *XY*-plane in increments of 2%, to examine the effect of strain on the electronic and mechanical properties of the predicted 2D borides. Although pure density functional theory (DFT) calculation will underestimate the band gap of semiconductors, the calculated trends are expected to be reliable. Therefore, we expect that DFT can rather reliably predict the competition of the energy levels of near-band-edge state in 2D borides.[59] Crystal orbital Hamilton population (COHP) calculations are performed to investigate the bond strength in the predicted compounds using the Local Orbital Basis Suite Towards Electronic-Structure Reconstruction (LOBSTER) code with the pbeVaspFit2015 basis set.[60−62] To evaluate the bond strength, it is assumed that the bond connected two atoms by springs.[63] The spring or force constant is a 3×3 matrix, which can be obtained from the output results of phonon calculations. The diffusion energy barriers along different migration pathways of Li^+ or Na^+ on 2D borides were explored using the climbing-image nudged elastic band (CI-NEB) method.[64]

RESULTS AND DISCUSSION

Stabilities and Structures of Predicted Ternary Borides. A series of layered ternary borides with formulas M_2AB, M_2AB_2, and M_3AB_4 were obtained through employing the search approach schemed in Figure 2. Variable-composition searches in ternary systems confirmed that Ti_2InB_2,[24] Hf_2InB_2, Hf_2SnB_2, Zr_2TlB_2, Zr_2PbB_2, Zr_2InB_2, Hf_3PB_4 Zr_3CdB_4, Hf_2BiB, and Hf_2PbB are thermodynamically stable with respect to their

https://dx.doi.org/10.1021/acs.chemmater.0c02139
Chem. Mater. 2020, 32, 6947−6957

any known competing isochemical phase assemblages, as shown in Figure 3. The M_2AB_2 borides including Zr_2InB_2, Zr_2PbB_2, Zr_2TlB_2, Hf_2InB_2, and Hf_2SnB_2 share the same crystal structure with Ti_2InB_2.[24] Furthermore, Hf_3PB_4 and Zr_3CdB_4 are identified as a new type of borides ("314" phases), which have the same space group as Ti_2InB_2 ($P\bar{6}m2$, No. 187) but exhibit a different structure type with thicker M−B layers (with five layers of M and B) than those in Ti_2InB_2. Moreover, borides Hf_2BiB and Hf_2PbB (M_2AB phases) show identical structural features with the traditional M_2AX phases (e.g., Ti_2AlC). The structures of those newly predicted thermodynamically stable ternary borides are shown in Figures 2 and S1 (Supporting Information). The calculated lattice parameters and atomic positions in predicted ternary borides are listed in Table S2 (Supporting Information). The absence of imaginary frequency modes in phonon dispersion calculations (Figures S2−S4, Supporting Information) indicates that all predicted ternary borides are dynamically stable. Furthermore, the results of AIMD simulations at 900 K over the time scale of at least 10 ps (Figures S5 and S6, Supporting Information) present that the original atomic configurations remain intact, implying that the MAX phases are thermally stable.

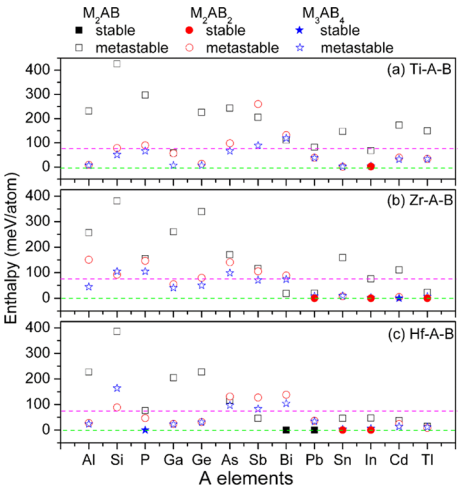

Figure 3. Enthalpies above the convex hull for the predicted ternary boride phases. The solid and hollow symbols indicate stable and metastable structures, respectively.

The enthalpies above the convex hull (δH) of all predicted materials are shown in Figure 3 and listed in Table S3 (Supporting Information). In total, 64 new borides show δH within 70 meV/atom that could be easily overcome by thermodynamic work, such as temperature, pressure, chemical and surface energy, etc.[65] For the Ti−A−B system (Figure 3a and Table S3, Supporting Information), δH of most 211 phases, except Ti_2InB (68 meV/atom), are far from the convex hull. While for 212 and 314 phases, there are 8 and 11 predicted compounds, whose δH are within 70 meV/atom. Furthermore, Ti_2SnB_2, Ti_3SnB_4, and Ti_3InB_4 even show a δH as small as 5 meV/atom. These results indicate that the 211 prototype of conventional MAX phases is unfavored in the Ti−A−B system. On the other hand, Ti_2AB_2 and Ti_3AB_4 systems are dramatically stabilized by the B−B bonding relative to conventional MAX phases. For the Zr−A−B and Hf−A−B systems, the stability of 211 phases is significantly improved relative to that of Ti_2AB phases. There are not only 11 compounds that have δH smaller than 70 meV/atom but two thermodynamically stable 211 phases of Hf_2BiB and Hf_2PbB. As revealed in Table S3 (Supporting Information), the stability of 212 and 314 phases in Zr−A−B and Hf−A−B systems is comparable to that in the Ti−A−B system. Fifteen 212 compounds and seventeen 314 compounds show δH values smaller than 70 meV/atom. Dynamical stabilities of some metastable structures, such as Hf_3InB_4, Hf_3SnB_4, Zr_2PbB, Zr_2BiB, and Zr_3PbB_4, are shown in Figures S3−S6 (Supporting Information). The calculated band structures (Figure S7, Supporting Information) reveal that the predicted borides possess metallic features, a typical characteristic of MAX phases.

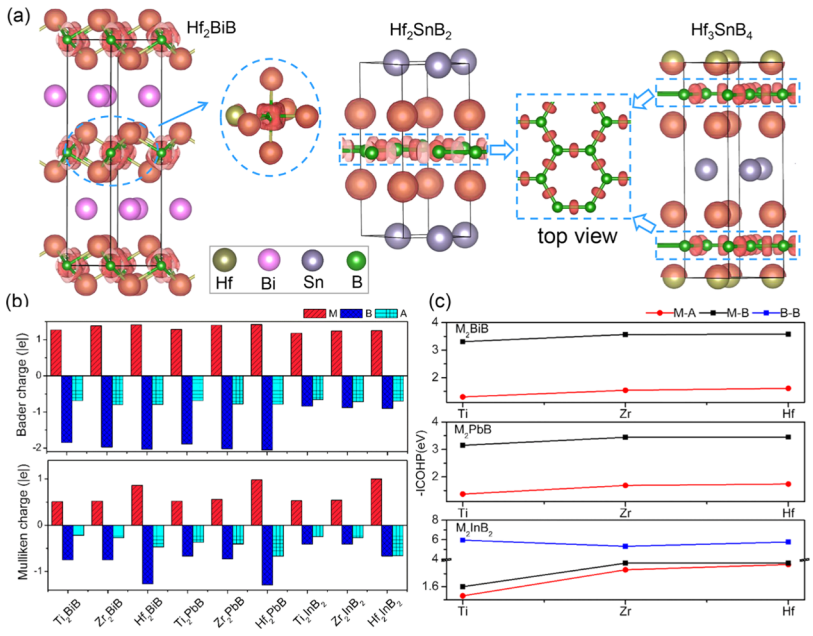

Figure 4. (a) Calculated three-dimensional (3D) isosurfaces of the electron localization function (ELF) plotted with a value of isosurface 0.75, (b) Bader and Mulliken charges, and (c) integrated crystal orbital Hamilton population (ICOHP) of M_2BiB, M_2PbB, and M_2InB_2 (M = Ti, Zr, and Hf).

https://dx.doi.org/10.1021/acs.chemmater.0c02139
Chem. Mater. 2020, 32, 6947−6957

The above results demonstrate that Hf with lower electronegativity (1.16 eV, compared to 1.38 eV of Ti) is more inclined to constitute 211 boron-containing conventional MAX phases. This conclusion is validated by the calculated thermodynamic stability of Hf_2BiB and Hf_2PbB with conventional 211 composition and structure (space group $P6_3/mmc$, No. 194). It is noteworthy that four metastable phases of Hf_2BiB and Hf_2PbB were also predicted with the hexagonal (space group $P\bar{6}m2$, no. 187) and trigonal (space group $R3m$, no. 160) structures (shown in Figure S2, Supporting Information). Although $R3m$ is not a subgroup of conventional MAX phases $P6_3/mmc$ (no. 194), the local topological structures of $R3m$ Hf_2BiB and Hf_2PbB exhibit the typical features of 211 MAX phases: strong M−B bonding and weak metallic M−A bonding, stacking of M atoms following hexagonal AB ordering in the M_2B layer and B atoms sitting at the center of M octahedra.

To further analyze the nature stability of ternary boride phases, the electron localization function (ELF), bonding strengths, and Bader and Mulliken charges of predicted structures were calculated. The ELF results of Hf_2BiB, Hf_2SnB_2, and Hf_3SnB_4 are shown in Figure 4a as examples. One can see that electron accumulation occurs around B atoms in Hf_2BiB, which suggests a significant electron transfer from Hf to B atoms. Bader and Mulliken charge analyses offer methodologies to quantitatively estimate the extent of charge transfer between atoms.[66,67] Therefore, the electron transfer between atoms in Hf_2BiB can be proved by the calculated Bader charges (Hf: +1.41|e|, Bi: −0.79|e| and B: −2.03|e|) and Mulliken charges (Hf: +0.86|e|, Bi: −0.47|e|, and B: −1.27|e|) (Table S4, Supporting Information). Using the structures of stable Hf_2BiB and Hf_2PbB as prototypes, the structures and Bader and Mulliken charges of Zr_2BiB, Zr_2PbB, Ti_2BiB, and Ti_2PbB were constructed and relaxed. The calculated Bader and Mulliken charges (Figure 4b and Table S4) indicate that significant electron transfer from M to B atoms appears in all cases. In each prototype, Hf atoms donate the most electrons to B, then Zr follows, and Ti supplies the least, which is consistent with the damping trend of electronegativity difference ($\Delta\chi$) of $\Delta\chi$(B−Hf) > $\Delta\chi$(B−Zr) > $\Delta\chi$(B−Ti). As is known, the stronger the charge separation of the M−B atoms, i.e., the greater the polarity of the M−B bond, the more exothermic is the formation of the compound. Therefore, the ionic strength of Hf−B bonds should be higher than that of Zr−B and Ti−B bonds. Furthermore, the spin−orbit coupling (SOC) effect was considered in the electronic structure calculations for Hf-based MAX phases. The calculations results (Figure S7) show that some crossing points near the Fermi level in the calculated band structures without considering SOC get opened upon the consideration of the SOC effect. Consequently, the lower electronegativity of Hf atoms might be a direct consequence of the relativistic effect of heavy Hf atoms.[68]

Previous studies have shown that the strength of M−B bonds in the carbide MAX phases has significant covalent contributions.[69,70] To estimate the covalent bond strength in those predicted phases, integrated crystal orbital Hamilton population (ICOHP)[60−62] and force constant calculations were carried out. Both the calculated ICOHP values and force constants of M−B bonds are much stronger than those of M−A bonds in each predicted 211 phase (Figure 4c and Table S4). The ICOHP and force constants values of Ti_2AlC and Ti_3AlC_2 reported by Khazaei et al.[69] and calculated values of some typical binary phases (e.g., TiB_2, Hf_2B, Hf_2Bi, etc.) are listed in Table S4 for comparison. From the comparison of these calculation results, we can conclude that the M−B bond in the 211 B-based MAX phases has a strong covalent bonding component. Furthermore, the covalent strengths of Hf−B bonds are slightly stronger than those of Ti−B and Zr−B bonds. Therefore, it is expected that the enhanced ionic and covalent components of the Hf−B bonds in the 211 phases are the origin of the higher stability of the BHf_6 octahedron than that of the BZr_6 and BTi_6 octahedra.

Most of the layered ternary borides (Hf_2InB_2, Hf_2SnB_2, Zr_2TlB_2, Zr_2PbB_2, Zr_2InB_2, Hf_3PB_4, Hf_3InB_4, Hf_3SnB_4, Zr_3CdB_4, and Zr_3PbB_4) obtained in this research share the same symmetry (space group $P\bar{6}m2$, No. 187) and local structure with Ti_2InB_2. The ELF of Hf_2SnB_2 and Hf_3SnB_4 shown in Figure 4a confirms that the two-dimensional B layers with strong covalent B−B bonds contribute greatly to the stability of the 212 and 314 phases. Bader and Mulliken charges and ICOHPs of Ti_2InB_2, Zr_2InB_2, and Hf_2InB_2 were calculated and are shown in Figure 4b,c. The calculated Bader charges for B atoms in Ti_2InB_2, Zr_2InB_2, and Hf_2InB_2 are −0.86|e|, −0.89|e|, and −0.90|e|, respectively. These results indicate that the ionic contribution of M−B bonds in 212 phases would be much weaker than those in 211 phases. Meanwhile, the calculated ICOHP values of B−B bonds of Ti_2InB_2, Zr_2InB_2, and Hf_2InB_2 can be as high as ∼6 eV, much higher than those calculated for M−B and M−In bonds. In addition, the calculated force constants for B−B, M−B, and M−A bonds in 212 phases follow the order B−B > M−B > M−A. Therefore, the improved stability of these phases with the compositions of M_2AB_2 and M_3AB_4 is due to the strong covalent boron−boron bonding in the graphene-like boron layer. Consequently, one can conclude that there are two stabilization mechanisms in those discovered ternary borides: in 211 phases, the strong Hf−B bonds reinforce the stability; in 212 and 314 phases, the strong covalent B−B bonding in the boron layer stabilizes the overall structures. It is worth mentioning that graphene-like atom layers in the 212 and 314 phases cannot be formed in carbide or nitride MAX phases because the formation of more stable substances such as graphite or nitrogen gas is favored when the X (C or N)/M ratio is equal to or larger than 1. However, due to electron deficiency (the availability of vacant $2p_z$ orbital of boron), the single atomic layer of boron, i.e., borophene, cannot be a stable freestanding phase like graphene.[71] Instead, the graphene-like boron layer would be stabilized in boron-based 212 and 314 phases by as part of a sandwich structure with charge transfer from M to B. Equivalently, in the Zintl picture, transferring an electron to a boron atom makes it behave like a carbon atom (hence graphene layers of B atoms), and when an electron is transferred to carbon or nitrogen atom, it populates an antibonding orbital, weakening C−C or N−N bonding.

Properties of Boride MXenes with and without Functional Groups. The anisotropic bonding nature in these boron-based MAX phases makes it possible to produce 2D transition-metal borides, i.e., new MXenes through the removal of A layers. To unravel the possibility of exfoliating ternary borides to 2D materials, the bonding energies and separation energy ratios of the ternary borides along the [001] direction were evaluated except Hf_3PB_4 where the Hf−P bonding is too strong. The calculated separation energies of M/A interfaces are much weaker than those of M/B interfaces (Figure S8, Supporting Information), which are comparable to those for the conventional MAX phases and Ti_2InB_2 that can be engineered to produce MXenes experimentally. Furthermore, the calculated M/A-to-M/B separation energy ratios (the ratios between the separation energies of M/A and M/B interfaces)

https://dx.doi.org/10.1021/acs.chemmater.0c02139
Chem. Mater. 2020, 32, 6947−6957

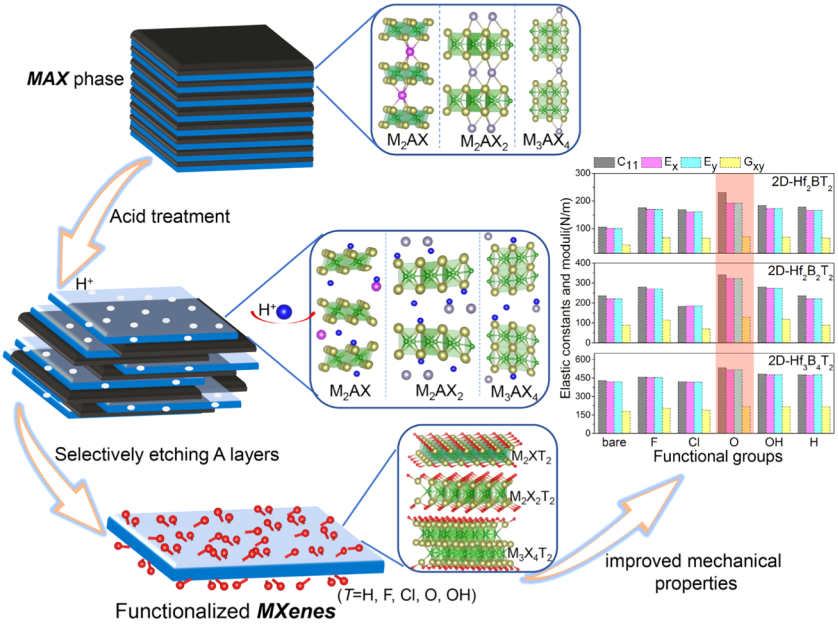

Figure 5. Schematic illustration of the exfoliation of A layers from the corresponding boron-based MAX phases and improved mechanical properties for the obtained functionalized MXenes.

are much smaller than the Ti/Al-to-Ti/C ratio (48%),[24] especially the calculated Hf/Bi-to-Hf/B ratio is only 24%. The total force constants for an atom (M, A, or B) counting all contributions from other atoms for some 211 and 212 phases were calculated and named as FC_A, FC_M, and FC_B (Table S4). The calculated FC_A of 211 and 212 phases in our work is much smaller than FC_M and FC_B. FC_A is a useful quantity to evaluate the possibility to exfoliate MAX phases into MXenes: the smaller the FC_A, the easier to remove A layers from their parents MAX phases. These calculated force constants in our work are comparable to those of MAX phases, which have already been experimentally exfoliated into 2D MXenes (Table S4). Therefore, our calculations suggest that it might be feasible to obtain 2D borides from predicted M_2AB, M_2AB_2, and M_3AB_4 by selective removal of A layers (illustrated in Figure 5).

Experimentally produced MXenes generally inherit rich surface functional groups T (T = OH, H, Cl, F, or O) from acids.[72−76] Therefore, it is of great importance to study the effect of those functional groups on the electronic structures and mechanical properties of the derived B-containing MXenes (Figure 5). It is found that three types of adsorption sites may be stable existing at the metal-terminated surfaces of MXene (Figure S9, Supporting Information).[77] As shown in Table S5 (Supporting Information), the hollow A site is the most stable adsorption site for all functional groups, except the preferred adsorptions of O atoms on hollow A and B sites of 2D M_2B_2 and M_3B_4. The OH-terminated configuration shows the most negative adsorption energy due to the existence of hydrogen bonds. Phonon dispersions and AIMD calculations signify that these 2D borides are dynamically and thermally stable, as illustrated in Figures S10−S15, Supporting Information. The calculated electronic structures (Figures S16−S20, Supporting Information) show the bands across the Fermi level, implying the intrinsic metallicity of all predicted 2D materials.

The in-plane planar elastic constants (C_{ij}), Young's moduli (E_x and E_y), and shear moduli (G_{xy}) together with Poisson's ratio (ν) of bare and functionalized MXenes were also calculated (Figures 5 and S21, Supporting Information). The elastic constants of all 2D borides meet the Born criteria[78] of mechanical stability, i.e., C_{11}, C_{22}, $C_{44} > 0$ and $C_{11}C_{22}-C_{12}^2 > 0$. Most of the functional MXenes, except 2D $M_2X_2Cl_2$, are characterized with higher in-plane planar Young's moduli than those bare ones. The highest Young's moduli and the largest Poisson's ratio of 2D M_2XO_2, $M_2X_2O_2$, and $M_3B_4O_2$ were highlighted with pink-shaded area in Figure 5, indicating their promising mechanical ductility and flexibility. In addition, the 2D borides with functional groups present higher in-plane stiffness than bare ones due to the higher shear moduli. As an in-plane anisotropy index, the in-plane elastic anisotropy was calculated by the following formula

$$A = E_x^{2D}/E_y^{2D} \quad (1)$$

The calculated values of A are all close to 1,[79] indicating that all 2D materials are in-plane elastically isotropic.

Influence of Strain on the Electronic Structures and Properties of Boron-Based MXenes. It is well known that external strain can affect on the electronic properties of 2D materials.[80−85] The stain effects on those newly discovered 2D borides were also studied. Here, the biaxial and uniaxial strains defined as $\varepsilon = (a - a_0)/a_0$ were applied to 2D Hf_2BT_2, 2D $Hf_2B_2T_2$, and 2D $Zr_2B_2T_2$ (T = F, Cl, and O), where a and a_0 are the lattice constants of the strained and unstrained unit cells, respectively. The illustration of applied stains on those structures can be found in Figure S22, Supporting Information. The ideal strength of a 2D material reflects the upper limit of an irreversible lattice resistance to a large strain.[79] The stress−strain curves under tensile strain are shown in Figures S23−S25, Supporting Information. One can see that all functionalized MXenes show much greater strength than the bare ones for all studied models. Besides, most of the predicted 2D materials are still metallic after application of strain, while 2D $Hf_2B_2F_2$ ($Hf_2B_2Cl_2$) and 2D $Zr_2B_2F_2$ ($Zr_2B_2Cl_2$) show a metal-to-semiconductor (metal-to-semimetal) transition under biaxial compressive strains, as concluded by Figures S26 and S27 (Supporting Information). The calculated band structures of 2D $Hf_2B_2F_2$ at strains of +2, 0, −4, and −8% are shown as an

https://dx.doi.org/10.1021/acs.chemmater.0c02139
Chem. Mater. 2020, 32, 6947−6957

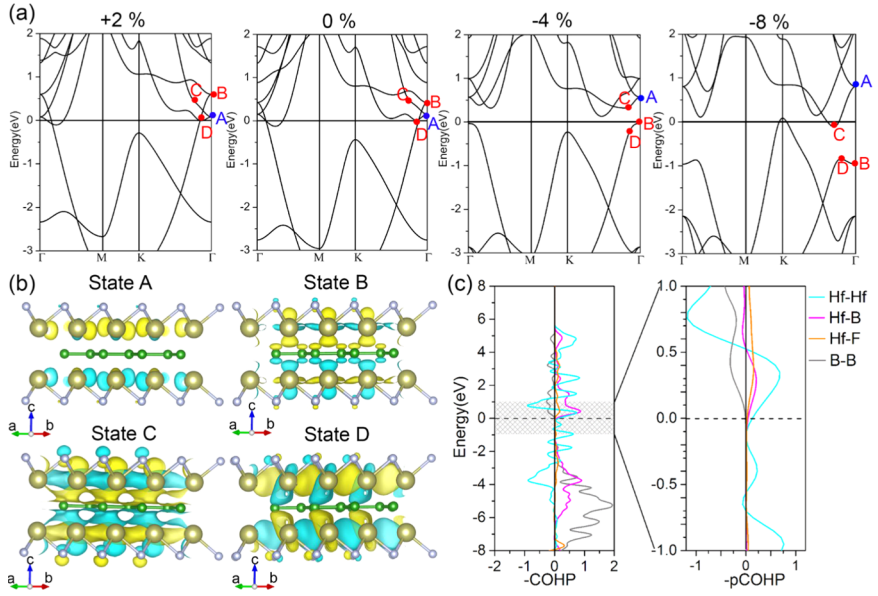

Figure 6. (a) Calculated band structures of 2D-$Hf_2B_2F_2$ with +2, 0, −4, and −8% biaxial strains. (b) Calculated wave function character of the near-band-edge states A−D at −4%. (c) Crystal orbital Hamilton population (COHP) analysis of Hf−Hf, Hf−B, B−B, and Hf−F interactions at −4%, and the enlarged drawing depicts the projected crystal orbital Hamilton population (pCOHP) of Hf−Hf ($d_{x^2-y^2}$ and d_{xy}), Hf−B (Hf-d_z^2, $d_{x^2-y^2}$, d_{xy}, and B-p_z), B−B (p_x, p_y, and p_z), and Hf−F (Hf-d_z^2 and F (p_z)) in the energy region from −1 to 1 eV.

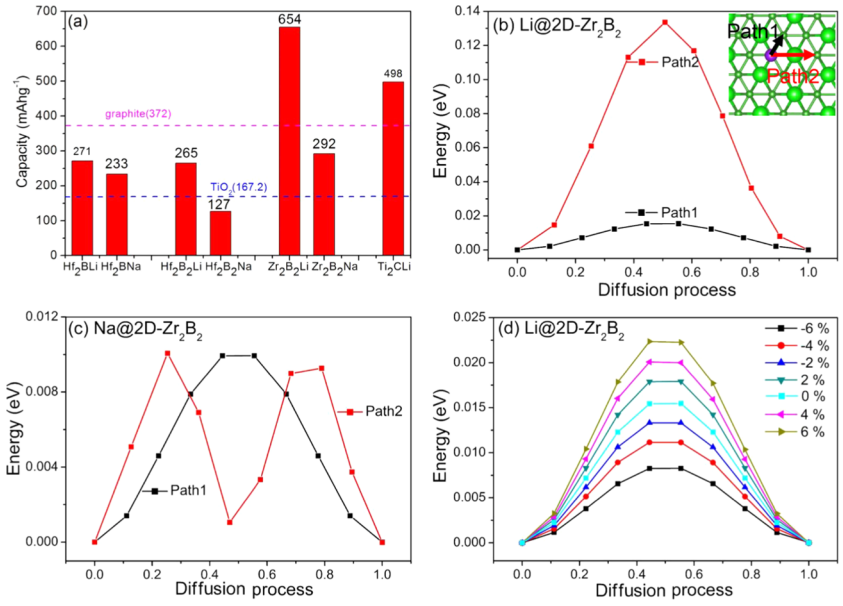

Figure 7. (a) Theoretical gravimetric capacities of the studied 2D MXenes. Calculated diffusion energy profiles of (b) Li@2D-Zr_2B_2 and (c) Na@2D-Zr_2B_2 (schematic representations of the diffusion paths are shown in the inset of b). (d) Calculated energy profiles of Li^+ diffusion on the surfaces of Zr_2B_2 under biaxial load conditions.

example in Figure 6a. The band gap under −4% strain is 0.17 eV, and it disappears with further increase of compressive strain. The band gap transition is attributed to the energy competition of the near-band-edge states (A−D) shown in Figure 6a. As the compressive strain increases, the energies of the states A increase gradually, while states B, C, and D decrease in energy.

To understand the realistic chemical bonding picture of the near-band-edge states A−D, the wave function characters at A−D points and the crystal orbital Hamilton population (COHP) were calculated.[61] The characteristics of wave functions shown in Figure 6b indicate that states A−D can be classified into two groups: antibonding state A and bonding states B, C, and D. The calculated orbital-resolved band structures and partial density of states (Figure S28, Supporting Information) show that antibonding state A is a mixture of Hf ($d_{x^2-y^2}$ + d_{xy}) and B (p_z), and bonding states B, C, and D mainly consist of the interactions of Hf ($d_{x^2-y^2}$ + d_{xy}), Hf (d_z^2), B (p_z), and F (p_z). The calculated COHP (Figure 6c) shows that Hf−B and B−B contribute to bonding states in the deep region from −8 to −2 eV. The enlarged drawing of projected COHP indicates that Hf−Hf interaction plays a major role in forming the bonding states B, C, and D and confirms the antibonding feature of state A near the Fermi level. The COHP analysis agrees well with the wave function character, which means that the nature of these

https://dx.doi.org/10.1021/acs.chemmater.0c02139
Chem. Mater. 2020, 32, 6947−6957

four states satisfies the Heitler−London exchange energy model.[86−88] Therefore, we can conclude that the bonding/antibonding state change under strain leads to the band gap transition.

Previous studies[6−9,14−16,89] revealed that the carbon- and nitrogen-based MAX phases can be promising anode material for Li-ion batteries due to their unique properties, including excellent electronic conductivity, low energy barrier for Li^+ migration, and high theoretical Li^+ storage capacity. Therefore, the adsorption and diffusion behaviors of Li^+/Na^+ on predicted 2D Hf_2B, Hf_2B_2, and Zr_2B_2 were calculated to explore their potential as anode materials for Li/Na-ion batteries. The adsorption behaviors of Li^+/Na^+ on both sides of boron-based MXenes were studied, and hollow A site was proved to be favorable for Li^+/Na^+ adsorption (Table S5, Supporting Information). As shown in Figures S29−S32 (Supporting Information), 2D Zr_2B_2 can accommodate up to three layers of Li atoms with negative adsorption energy, which corresponds to an ideal capacity of up to 654 mAh g^{-1}. This value is comparable to some commercial anode materials (e.g., 372 and 167.2 mAh g^{-1} for graphite and TiO_2, respectively, as shown in Figure 7a). Thus, 2D Zr_2B_2 was taken as a representative to explore its properties as a potential anode material in detail.

The diffusion behavior of the surface-adsorbed Li^+/Na^+ is crucial for evaluating the performance of an anode material. The possible diffusion pathways of Li^+ or Na^+ on the Zr_2B_2 surface were investigated using the climbing-image nudged elastic band (CI-NEB) method. As shown in Figure 7b,c, the calculated migration energy barriers of Li^+ and Na^+ on 2D Zr_2B_2 are 0.018 and 0.015 eV, respectively, which are lower than some typical commercial electrodes, such as TiO_2 (0.35−0.65 eV),[90,91] graphene (0.33 eV),[92] black phosphorus (0.084 eV),[93] Ti_3C_2 (0.07 eV),[10] and MoS_2 (0.25 eV).[94] Furthermore, we explored the biaxial strain effect on the diffusion behavior and average adsorption energies of $Li@Zr_2B_2$. Figure 7d shows that the calculated Li^+ diffusion energy barrier decreases as the compressive biaxial strain increases. It is suggested that Li^+ diffusion energy barrier can be efficiently modified by compressive strain. Overall, judging from the small Li^+ diffusion energy barrier, high Li^+ storage capacity, and the tunable diffusion energy barrier, Zr_2B_2 is an attractive candidate as a promising flexible Li-ion battery anode.

CONCLUSIONS

In summary, a series of layered ternary borides were predicted by employing evolutionary structure search using the USPEX code and then a systematic investigation of stabilities and electronic structures of predicted compounds and their derived 2D structures were conducted using first-principles calculations. All discovered borides show characteristics of MAX phases and can be classified into three types of prototypes with 212 (e.g., Hf_2InB_2, Hf_2SnB_2, Zr_2TlB_2, Zr_2PbB_2, and Zr_2InB_2), 314 (e.g., Hf_3PB_4 and Zr_3CdB_4), and 211 (Hf_2BiB and Hf_2PbB) compositions. It is revealed that there exist two kinds of stabilization units in the boron-containing MAX phases: graphene-like boron layer in 212 and 314 phases and M−B octahedra with enhanced stability in 211 phases. The stabilities and small separation energy ratios of the predicted boron-based MAX phases indicate the high likelihood of synthesizing new MXenes experimentally. According to the calculated phonon spectra and elastic constants, the predicted boride MXenes are dynamically and mechanically stable, and the surface functionalization could significantly improve their mechanical properties. Although most of boride MXenes are metallic, appropriate biaxial compressive strain can transform 2D $Hf_2B_2F_2$ ($Hf_2B_2Cl_2$) and 2D $Zr_2B_2F_2$ ($Zr_2B_2Cl_2$) from metal to semiconductor (semimetal). 2D Zr_2B_2 exhibits high theoretical capacity and low migration energy barrier for Li^+/Na^+, demonstrating great prospects of those predicted materials for energy storage. The present study extends the family of MAX phases and MXenes to boron-based system and encourage researchers to pursue other members of this fascinating class of compounds.

ASSOCIATED CONTENT

Supporting Information

The Supporting Information is available free of charge at https://pubs.acs.org/doi/10.1021/acs.chemmater.0c02139.

Settings for the calculations of adsorption and diffusion behaviors on 2D borides; crystal structure, calculated phonon spectra, electronic structures, and equilibrium structures of AIMD simulations of predicted boron-based MAX phases (Figures S1−S7); calculated bonding energies and separation energy ratios at different interfaces of new MAX phases (Figure S8); different configuration models of 2D borides with functional groups (Figure S9); calculated phonon spectra, electronic structures, and equilibrium structures of AIMD simulations of predicted 2D borides (Figures S10−S20); calculated mechanical properties of 2D borides (Figure S21); schematic illustration of applied strain and calculated stress−strain curves of 2D borides (Figures S22−S25); calculated band structures of 2D borides under compressive strains (Figures S26−S28); considered adsorption sites, diffusion pathways, most stable adsorption configurations and adsorption energies for Li^+ and Na^+ on 2D Hf_2B, 2D Hf_2B_2, and 2D Zr_2B_2 (Figures S29−S32); PAW pseudopotentials of all used elements (Table S1); crystal structure information and calculated energies of predicted boron-based MAX phases (Table S2); calculated enthalpies above the convex hull of all predicted structures (Table S3); calculated Bader charges, Mulliken charges, and bond strengths of predicted structures (Table S4); and calculated adsorption energies of functional groups on 2D borides (Table S5) (PDF)

AUTHOR INFORMATION

Corresponding Authors

Junjie Wang − *State Key Laboratory of Solidification Processing and International Center for Materials Discovery, School of Materials Science and Engineering, Northwestern Polytechnical University, Xi'an, Shaanxi 710072, People's Republic of China; Materials Research Center for Element Strategy, Tokyo Institute of Technology, Yokohama, Kanagawa 226-8503, Japan;* orcid.org/0000-0002-6428-2233; Email: wang.junjie@nwpu.edu.cn

Artem R. Oganov − *State Key Laboratory of Solidification Processing and International Center for Materials Discovery, School of Materials Science and Engineering, Northwestern Polytechnical University, Xi'an, Shaanxi 710072, People's Republic of China; Skolkovo Innovation Center, Skolkovo Institute of Science and Technology, Moscow 143026, Russia;* orcid.org/0000-0001-7082-9728; Email: a.oganov@skoltech.ru

https://dx.doi.org/10.1021/acs.chemmater.0c02139
Chem. Mater. 2020, 32, 6947−6957

Authors

Nanxi Miao − *State Key Laboratory of Solidification Processing and International Center for Materials Discovery, School of Materials Science and Engineering, Northwestern Polytechnical University, Xi'an, Shaanxi 710072, People's Republic of China*

Yutong Gong − *State Key Laboratory of Solidification Processing and International Center for Materials Discovery, School of Materials Science and Engineering, Northwestern Polytechnical University, Xi'an, Shaanxi 710072, People's Republic of China*

Jiazhen Wu − *Materials Research Center for Element Strategy, Tokyo Institute of Technology, Yokohama, Kanagawa 226-8503, Japan*

Haiyang Niu − *State Key Laboratory of Solidification Processing and International Center for Materials Discovery, School of Materials Science and Engineering, Northwestern Polytechnical University, Xi'an, Shaanxi 710072, People's Republic of China*

Shiyao Wang − *State Key Laboratory of Solidification Processing and International Center for Materials Discovery, School of Materials Science and Engineering, Northwestern Polytechnical University, Xi'an, Shaanxi 710072, People's Republic of China*

Kun Li − *State Key Laboratory of Solidification Processing and International Center for Materials Discovery, School of Materials Science and Engineering, Northwestern Polytechnical University, Xi'an, Shaanxi 710072, People's Republic of China*

Tomofumi Tada − *Materials Research Center for Element Strategy, Tokyo Institute of Technology, Yokohama, Kanagawa 226-8503, Japan; Kyushu University Platform of Inter/Transdisciplinary Energy Research, Kyushu University, Nishi-ku, Fukuoka 819-0395, Japan*

Hideo Hosono − *Materials Research Center for Element Strategy, Tokyo Institute of Technology, Yokohama, Kanagawa 226-8503, Japan;* orcid.org/0000-0001-9260-6728

Complete contact information is available at: https://pubs.acs.org/10.1021/acs.chemmater.0c02139

Author Contributions

All authors have given approval to the final version of the manuscript.

Notes

The authors declare no competing financial interest.

■ ACKNOWLEDGMENTS

This work was supported by National Natural Science Foundation of China (grant no. 51872242), the Fundamental Research Funds for the Central Universities (no. D5000200142), and the Research Fund of the State Key Laboratory of Solidification Processing (NPU), China (grant no. 2019-TS-08). T.T. and H.H. were supported by the Ministry of Education, Culture, Sports, Science and Technology (MEXT) through the Element Strategy Initiative to Form Core Research Center and supported by the Japan Society for the Promotion of Science (JSPS) through a Grant-in-Aid for Scientific Research (S) No. 17H06153. A.R.O. thanks Russian Science Foundation (grant no. 19-72-30043).

■ REFERENCES

(1) Barsoum, M. W. The MN+1AXN Phases: A New Class of Solids; Thermodynamically Stable Nanolaminates. *Prog. Solid State Chem* **2000**, *28*, 201−281.

(2) Anasori, B.; Lukatskaya, M. R.; Gogotsi, Y. 2D Metal Carbides and Nitrides (MXenes) for energy storage. *Nat. Rev. Mater.* **2017**, *2*, 16098.

(3) Guo, Z. L.; Zhou, J.; Si, C.; Sun, Z. M. Flexible Two-Dimensional Tin+1Cn (n = 1, 2 and 3) and Their Functionalized MXenes Predicted by Density Functional Theories. *Phys. Chem. Chem. Phys.* **2015**, *17*, 15348−15354.

(4) Sun, Z. M.; Music, D.; Ahuja, R.; Li, S.; Schneider, J. M. Bonding and Classification of Nanolayered Ternary Carbides. *Phys. Rev. B* **2004**, *70*, No. 092102.

(5) Naguib, M.; Kurtoglu, M.; Presser, V.; Lu, J.; Niu, J.; Heon, M.; Hultman, L.; Gogotsi, Y.; Barsoum, M. W. Two-Dimensional Nanocrystals Produced by Exfoliation of Ti3AlC2. *Adv. Mater.* **2011**, *23*, 4248−4253.

(6) Ghidiu, M.; Lukatskaya, M. R.; Zhao, M. Q.; Gogotsi, Y.; Barsoum, M. W. Conductive Two-Dimensional Titanium Carbide 'clay' with High Volumetric Capacitance. *Nature* **2014**, *516*, 78.

(7) Khazaei, M.; Ranjbar, A.; Arai, M.; Sasaki, T.; Yunoki, S. Electronic Properties and Applications of MXenes: a Theoretical Review. *J. Mater. Chem. C* **2017**, *5*, 2488−2503.

(8) Lv, L. P.; Guo, C. F.; Sun, W. W.; Wang, Y. Strong Surface-Bound Sulfur in Carbon Nanotube Bridged Hierarchical Mo2C-Based MXene Nanosheets for Lithium-Sulfur Batteries. *Small* **2019**, *15*, No. 1804338.

(9) Naguib, M.; Halim, J.; Lu, J.; Cook, K. M.; Hultman, L.; Gogotsi, Y.; Barsoum, M. W. New Two-Dimensional Niobium and Vanadium Carbides as Promising Materials for Li-ion Batteries. *J. Am. Chem. Soc.* **2013**, *135*, 15966−15969.

(10) Tang, Q.; Zhou, Z.; Shen, P. W. Are MXenes Promising Anode Materials for Li ion batteries? Computational Studies on Electronic Properties and Li Storage Capability of Ti3C2 and Ti3C2X2 (X = F, OH) monolayer. *J. Am. Chem. Soc.* **2012**, *134*, 16909−16916.

(11) Wu, Y. T.; Nie, P.; Wu, L. Y.; Dou, H.; Zhang, X. G. 2D MXene/SnS2 Composites as High-Performance Anodes for Sodium Ion Batteries. *Chem. Eng. J.* **2018**, *334*, 932−938.

(12) Yadav, A.; Dashora, A.; Patel, N.; Miotello, A.; Press, M.; Kothari, D. C. Study of 2D MXene Cr2C Material for Hydrogen Storage Using Density Functional Theory. *Appl. Surf. Sci.* **2016**, *389*, 88−95.

(13) Tang, X.; Guo, X.; Wu, W. J.; Wang, G. X. 2D Metal Carbides and Nitrides (MXenes) as High Performance Electrode Materials for Lithium-Based Batteries. *Adv. Energy Mater.* **2018**, *8*, No. 1801897.

(14) Yang, Z. F.; Zheng, Y. P.; Li, W. L.; Zhang, J. P. Investigation of Two-Dimensional Hf-based MXenes as the Anode Materials for Li/Na-Ion Batteries: A DFT Study. *J. Comput. Chem.* **2019**, *40*, 1352−1359.

(15) Wang, B.; Zhou, A.; Liu, F.; Cao, J.; Wang, L.; Hu, Q. Carbon Dioxide Adsorption of Two-Dimensional Carbide MXenes. *J. Adv. Ceram.* **2018**, *7*, 237−245.

(16) Er, D.; Li, J.; Naguib, M.; Gogotsi, Y.; Shenoy, V. B. Ti3C2 MXene as a High Capacity Electrode Material for Metal (Li, Na, K, Ca) Ion Batteries. *ACS Appl. Mater. Interfaces* **2014**, *6*, 11173−11179.

(17) Anasori, B.; Xie, Y.; Beidaghi, M.; Lu, J.; Hosler, B. C.; Hultman, L.; Kent, P. R. C.; Gogotsi, Y.; Barsoum, M. W. Two-Dimensional, Ordered, Double Transition Metals Carbides (MXenes). *ACS Nano* **2015**, *9*, 9507−9516.

(18) Xie, Y.; Naguib, M.; Mochalin, V. N.; Barsoum, M. W.; Gogotsi, Y.; Yu, X.; Nam, K.; Yang, X. Q.; Kolesnikov, A. I.; Kent, P. R. C. Role of Surface Structure on Li-Ion Energy Storage Capacity of Two-Dimensional Transition-Metal Carbides. *J. Am. Chem. Soc.* **2014**, *136*, 6385−6494.

(19) Jiang, Y.; Wu, X.; Yan, Y.; Luo, S.; Li, X.; Huang, J.; Zhang, H.; Yang, D. Coupling PtNi Ultrathin Nanowires with MXenes for Boosting Electrocatalytic Hydrogen Evolution in Both Acidic and Alkaline Solutions. *Small* **2019**, *15*, No. 1805474.

(20) Su, T.; Hood, Z. D.; Naguib, M.; Bai, L.; Luo, S.; Rouleau, C. M.; Ivanov, I. N.; Ji, H.; Qin, Z.; Wu, Z. 2D/2D Heterojunction of Ti3C2/g-C3N4 Nanosheets for Enhanced Photocatalytic Hydrogen Evolution. *Nanoscale* **2019**, *11*, 8138−8149.

(21) Shahzad, F.; Alhabeb, M.; Hatter, C. B.; Anasori, B.; Hong, S. M.; Koo, C. M.; Gogotsi, Y. Electromagnetic Interference Shielding with 2D Transition Metal Carbides (MXenes). *Science* **2016**, *353*, 1137−1140.

(22) Cao, M.; Cai, Y.; He, P.; Shu, J.; Cao, W.; Yuan, J. 2D MXenes: Electromagnetic Property for Microwave Absorption and Electromagnetic Interference Shielding. *Chem. Eng. J.* **2019**, *359*, 1265−1302.

(23) Han, M.; Yin, X.; Hantanasirisakul, K.; Li, X.; Iqbal, A.; Hatter, C. B.; Anasori, B.; Koo, C. M.; Torita, T.; Soda, Y.; Zhang, L.; Cheng, L.; Gogotsi, Y. Anisotropic MXene Aerogels with a Mechanically Tunable Ratio of Electromagnetic Wave Reflection to Absorption. *Adv. Optical Mater.* **2019**, *7*, No. 1900267.
(24) Wang, J. J.; Ye, T. N.; Gong, Y. T.; Wu, J. Z.; Miao, N. M.; Tada, T.; Hosono, H. Discovery of Hexagonal Ternary Phase Ti2InB2 and Its Evolution to Layered Boride TiB. *Nat. Commun.* **2019**, *10*, No. 2284.
(25) Horlait, D.; Middleburgh, S. C.; Chroneos, A.; Lee, W. E. Synthesis and DFT Investigation of New Bismuth-Containing MAX Phases. *Sci. Rep.* **2016**, *6*, No. 18829.
(26) Kim, K.; Chen, C.; Nishio-Hamane, D.; Okubo, M.; Yamada, A. Topochemical Synthesis of Phase-Pure Mo2AlB2 through Staging Mechanism. *Chem. Commun.* **2019**, *55*, 9295−9298.
(27) Kota, S.; Zapata-Solvas, E.; Ly, A.; Lu, J.; Elkassabany, O.; Huon, A.; Lee, W. E.; Hultman, L.; May, S. J.; Barsoum, M. W. Synthesis and Characterization of an Alumina Forming Nanolaminated Boride: MoAlB. *Sci. Rep.* **2016**, *6*, No. 26475.
(28) Lapauw, T.; Halim, J.; Lu, J.; Cabioc'h, T.; Hultman, L.; Barsoum, M. W.; Lambrinou, K.; Vleugels, J. Synthesis of the Novel Zr3AlC2 MAX Phase. *J. Eur. Ceram. Soc.* **2016**, *36*, 943−947.
(29) Liu, Z.; Wu, E.; Wang, J.; Qian, Y.; Xiang, H.; Li, X.; Jin, Q.; Sun, G.; Chen, X.; Wang, J.; Li, M. Crystal Structure and Formation Mechanism of (Cr2/3Ti1/3)3AlC2 MAX Phase. *Acta Mater.* **2014**, *73*, 186−193.
(30) Alhabeb, M.; Maleski, K.; Mathis, T. S.; Sarycheva, A.; Hatter, C. B.; Uzun, S.; Levitt, A.; Gogotsi, Y. Selective Etching of Silicon from Ti3SiC2 (MAX) to Obtain 2D Titanium Carbide (MXene). *Angew. Chem., Int. Ed.* **2018**, *57*, 5444−5448.
(31) Sokol, M.; Natu, V.; Kota, S.; Barsoum, M. W. On the Chemical Diversity of the MAX Phases. *Trends Chem.* **2019**, *1*, 210−223.
(32) Ling, C.; Tian, W. B.; Zhang, P.; Zheng, W.; Zhang, Y. M.; Sun, Z. M. Synthesis and Formation Mechanism of Titanium Lead Carbide. *J. Adv. Ceram.* **2018**, *7*, 178−183.
(33) Zhang, B.; Zhou, J.; Guo, Z.; Peng, Q.; Sun, Z. Two-dimensional chromium boride MBenes with high HER catalytic activity. *Appl. Surf. Sci.* **2020**, *500*, No. 144248.
(34) Yu, Y.; Zhou, J.; Sun, Z. Novel 2D Transition-Metal Carbides: Ultrahigh Performance Electrocatalysts for Overall Water Splitting and Oxygen Reduction. *Adv. Funct. Mater.* **2020**, No. 2000570.
(35) Khazaei, M.; Arai, M.; Sasaki, T.; Estili, M.; Sakka, Y. Trends in Electronic Structures and Structural Properties of MAX Phases: a First-Principles Study on M2AlC (M = Sc, Ti, Cr, Zr, Nb, Mo, Hf, or Ta), M2AlN, and Hypothetical M2AlB Phases. *J. Phys.: Condens. Matter* **2014**, *26*, No. 505503.
(36) Allen, L. C. Electronegativity is the Average One-Electron Energy of the Valence-Shell Electrons in Ground-State Free Atoms. *J. Am. Chem. Soc.* **1989**, *111*, 9003−9014.
(37) Mann, J. B.; Meek, T. L.; Allen, L. C. Configuration Energies of the Main Group Elements. *J. Am. Chem. Soc.* **2000**, *122*, 2780−2783.
(38) Mann, J. B.; Meek, T. L.; Knight, E. T.; Capitani, J. F.; Allen, L. C. Configuration Energies of the d-Block Elements. *J. Am. Chem. Soc.* **2000**, *122*, 5132−5137.
(39) Ade, M.; Hillebrecht, H. Ternary Borides Cr2AlB2, Cr3AlB4, and Cr4AlB6: The First Members of the Series (CrB2)nCrAl with n = 1, 2, 3 and a Unifying Concept for Ternary Borides as MAB-Phases. *Inorg. Chem.* **2015**, *54*, 6122−6135.
(40) Kota, S.; Sokol, M.; Barsoum, M. W. A Progress Report on the MAB Phases: Atomically Laminated, Ternary Transition Metal Borides. *Int. Mater. Rev.* **2019**, *65*, 226−255.
(41) Alameda, L. T.; Lord, R. W.; Barr, J. A.; Moradifar, P.; Metzger, Z. P.; Steimle, B. C.; Holder, C. F.; Alem, N.; Sinnott, S. B.; Schaak, R. E. Multi-Step Topochemical Pathway to Metastable Mo2AlB2 and Related Two-Dimensional Nanosheet Heterostructures. *J. Am. Chem. Soc.* **2019**, *141*, 10852−10861.
(42) Alameda, L. T.; Moradifar, P.; Metzger, Z. P.; Alem, N.; Schaak, R. E. Topochemical Deintercalation of Al from MoAlB: Stepwise Etching Pathway, Layered Intergrowth Structures, and Two-Dimensional MBene. *J. Am. Chem. Soc.* **2018**, *140*, 8833−8840.
(43) Guo, Z. L.; Zhou, J.; Sun, Z. M. New Two-Dimensional Transition Metal Borides for Li Ion Batteries and Electrocatalysis. *J. Mater. Chem. A* **2017**, *5*, 23530−23535.
(44) Jia, J.; Li, B.; Duan, S.; Cui, Z.; Gao, H. Monolayer MBenes: Prediction of Anode Materials for High-Performance Lithium/Sodium Ion Batteries. *Nanoscale* **2019**, *11*, 20307−20314.
(45) Yuan, H.; Li, Z.; Yang, J. Transition-Metal Diboride: a New Family of Two-Dimensional Materials Designed for Selective CO2 Electroreduction. *J. Phys. Chem. C* **2019**, *123*, 16294−16299.
(46) Jiang, Z.; Wang, P.; Jiang, X.; Zhao, J. MBene (MnB): a New Type of 2D Metallic Ferromagnet with High Curie Temperature. *Nanoscale Horiz* **2018**, *3*, 335−341.
(47) Zhu, Q.; Jung, D. Y.; Oganov, A. R.; Glass, C. W.; Gatti, C.; Lyakhov, A. O. Stability of Xenon Oxides at High Pressures. *Nat. Chem.* **2013**, *5*, 61−65.
(48) Niu, H. Y.; Oganov, A. R.; Chen, X. Q.; Li, D. Z. Prediction of Novel Stable Compounds in the Mg-Si-O System Under Exoplanet Pressures. *Sci. Rep.* **2015**, *5*, No. 18347.
(49) Wang, J. J.; Hanzawa, K.; Hiramatsu, H.; Kim, J.; Umezawa, N.; Iwanaka, K.; Tada, T.; Hosono, H. Exploration of Stable Strontium Phosphide-Based Electrides: Theoretical Structure Prediction and Experimental Validation. *J. Am. Chem. Soc.* **2017**, *139*, 15668−15680.
(50) Jain, A.; Ong, S. P.; Hautier, G.; Chen, W.; Richards, W. D.; Dacek, S.; Cholia, S.; Gunter, D.; Skinner, D.; Ceder, G.; Persson, K. A. Commentary: The Materials Project: A Materials Genome Approach to Accelerating Materials Innovation. *APL Mater.* **2013**, *1*, No. 011002.
(51) Glass, C. W.; Oganov, A. R.; Hansen, N. USPEX—Evolutionary Crystal Structure Prediction. *Comput. Phys. Commun.* **2006**, *175*, 713−720.
(52) Oganov, A. R.; Glass, C. W. Crystal Structure Prediction Using Ab Initio Evolutionary Techniques: Principles and Applications. *J. Chem. Phys.* **2006**, *124*, No. 244704.
(53) Zhu, Q.; Li, L.; Oganov, A. R.; Allen, P. B. Evolutionary Method for Predicting Surface Reconstructions with Variable Stoichiometry. *Phys. Rev. B* **2013**, *87*, No. 195317.
(54) Kresse, G.; Furthmüller, J. Efficient Iterative Schemes for Ab Initio Total-Energy Calculations Using a Plane-Wave Basis Set. *Phys. Rev. B* **1996**, *54*, 11169−11186.
(55) Kresse, G.; Joubert, D. From Ultrasoft Pseudopotentials to the Projector Augmented-Wave Method. *Phys. Rev. B* **1999**, *59*, 1758.
(56) Perdew, J. P.; Burke, K.; Ernzerhof, M. Generalized Gradient Approximation Made Simple. *Phys. Rev. Lett.* **1996**, *77*, 3865−3868.
(57) Togo, A.; Tanaka, I. First Principles Phonon Calculations in Materials Science. *Scr. Mater.* **2015**, *108*, 1−5.
(58) Kresse, G.; Hafner, J. Ab Initio Molecular Dynamics for Liquid Metals. *Phys. Rev. B* **1993**, *47*, 558−561.
(59) Peng, X.; Wei, Q.; Copple, A. Strain-Engineered Direct-Indirect Band Gap Transition and Its Mechanism in Two-Dimensional Phosphorene. *Phys. Rev. B* **2014**, *90*, No. 085402.
(60) Deringer, V. L.; Tchougreeff, A. L.; Dronskowski, R. Crystal Orbital Hamilton Population (COHP) Analysis as Projected From Plane-Wave Basis Sets. *J. Phys. Chem. A* **2011**, *115*, 5461−5466.
(61) Maintz, S.; Deringer, V. L.; Tchougreeff, A. L.; Dronskowski, R. Analytic Projection from Plane-Wave and PAW Wavefunctions and Application to Chemical-Bonding Analysis in Solids. *J. Comput. Chem.* **2013**, *34*, 2557−2567.
(62) Maintz, S.; Deringer, V. L.; Tchougreeff, A. L.; Dronskowski, R. LOBSTER: A Tool to Extract Chemical Bonding from Plane-Wave Based DFT. *J. Comput. Chem.* **2016**, *37*, 1030−1035.
(63) Deringer, V. L.; Stoffel, R. P.; Wuttig, M.; Dronskowski, R. Vibrational Properties and Bonding Nature of Sb2Se3 and their Implications for Chalcogenide Materials. *Chem. Sci.* **2015**, *6*, 5255−5262.
(64) Mills, G.; Jonsson, H. Quantum and Thermal Effects in H2 Dissociative Adsorption: Evaluation of Free Energy Barriers in Multidimensional Quantum Systems. *Phys. Rev. Lett.* **1994**, *72*, 1124−1127.
(65) Sun, W.; Dacek, S. T.; Ong, S. P.; Hautier, G.; Jain, A.; Richards, W. D.; Gamst, A. C.; Persson, K. A.; Ceder, G. The Thermodynamic

https://dx.doi.org/10.1021/acs.chemmater.0c02139
Chem. Mater. 2020, 32, 6947−6957

Scale of Inorganic Crystalline Metastability. *Sci. Adv.* **2016**, *2*, No. e1600225.
(66) Henkelman, G.; Arnaldsson, A.; Jónsson, H. A Fast and Robust Algorithm for Bader Decomposition of Charge Density. *Comput. Mater. Sci.* **2006**, *36*, 354−360.
(67) Mulliken, R. S. Electronic Population Analysis on LCAO-MO Molecular Wave Functions. III. Effects of Hybridization on Overlap and Gross AO Populations. *J. Chem. Phys.* **1955**, *23*, 1833−1840.
(68) Pyykkö, P. Relativistic Effects in Chemistry: More Common than You Thought. *Annu. Rev. Phys. Chem.* **2012**, *63*, 45−64.
(69) Khazaei, M.; Ranjbar, A.; Esfarjani, K.; Bogdanovski, D.; Dronskowski, R.; Yunoki, S. Insights into Exfoliation Possibility of MAX Phases to MXenes. *Phys. Chem. Chem. Phys.* **2018**, *20*, 8579−8592.
(70) Khazaei, M.; Wang, J.; Estili, M.; Ranjbar, A.; Suehara, S.; Arai, M.; Esfarjani, K.; Yunoki, S. Novel MAB Phases and Insights into Their Exfoliation into 2D MBenes. *Nanoscale* **2019**, *11*, 11305−11314.
(71) Tominaka, S.; Ishibiki, R.; Fujino, A.; Kawakami, K.; Ohara, K.; Masuda, T.; Matsuda, I.; Hosono, H.; Kondo, T. Geometrical Frustration of B-H Bonds in Layered Hydrogen Borides Accessible by Soft Chemistry. *Chem* **2020**, *6*, 406−418.
(72) Li, G.; Jiang, K.; Zaman, S.; Xuan, J.; Wang, Z.; Geng, F. Ti3C2 Sheets with an Adjustable Surface and Feature Sizes to Regulate the Chemical Stability. *Inorg. Chem.* **2019**, *58*, 9397−9403.
(73) Sharma, G.; Naguib, M.; Feng, D.; Gogotsi, Y.; Navrotsky, A. Calorimetric Determination of Thermodynamic Stability of MAX and MXene Phases. *J. Phys. Chem. C* **2016**, *120*, 28131−28137.
(74) Verger, L.; Natu, V.; Carey, M.; Barsoum, M. W. MXenes: an Introduction of Their Synthesis, Select Properties, and Applications. *Trends Chem.* **2019**, *1*, 656−669.
(75) Wang, H. W.; Naguib, M.; Page, K.; Wesolowski, D. J.; Gogotsi, Y. Resolving the Structure of Ti3C2Tx MXenes through Multilevel Structural Modeling of the Atomic Pair Distribution Function. *Chem. Mater.* **2015**, *28*, 349−359.
(76) Sang, X.; Xie, Y.; Lin, M. W.; Alhabeb, M.; Van Aken, K. L.; Gogotsi, Y.; Kent, P. R. C.; Xiao, K.; Unocic, R. R. Atomic Defects in Monolayer Titanium Carbide (Ti3C2Tx) MXene. *ACS Nano* **2016**, *10*, 9193−9200.
(77) Khazaei, M.; Arai, M.; Sasaki, T.; Chung, C. Y.; Venkataramanan, N. S.; Estili, M.; Sakka, Y.; Kawazoe, Y. Novel Electronic and Magnetic Properties of Two-Dimensional Transition Metal Carbides and Nitrides. *Adv. Funct. Mater.* **2013**, *23*, 2185−2192.
(78) Born, M.; Huang, K.; Lax, M. Dynamical Theory of Crystal Lattices. *Am. J. Phys.* **1954**, *39*, 113−127.
(79) Fu, Z. H.; Zhang, Q. F.; Legut, D.; Si, C.; Germann, T. C.; Lookman, T.; Du, S. Y.; Francisco, J. S.; Zhang, R. F. Stabilization and Strengthening Effects of Functional Groups in Two-Dimensional Titanium Carbide. *Phys. Rev. B* **2016**, *94*, No. 104103.
(80) Lv, H. Y.; Lu, W. J.; Shao, D. F.; Liu, Y.; Sun, Y. P. Strain-Controlled Switch between Ferromagnetism and Antiferromagnetism in 1T-CrX2 (X = Se, Te) Monolayers. *Phys. Rev. B* **2015**, *92*, No. 214419.
(81) He, K.; Poole, C.; Mak, K. F.; Shan, J. Experimental Demonstration of Continuous Electronic Structure Tuning via Strain in Atomically Thin MoS2. *Nano Lett.* **2013**, *13*, 2931−2936.
(82) Scalise, E.; Houssa, M.; Pourtois, G.; Afanas'ev, V.; Stesmans, A. Strain-induced Semiconductor to Metal Transition in the Two-Dimensional Honeycomb Structure of MoS2. *Nano Res.* **2011**, *5*, 43−48.
(83) Siriwardane, E. M. D.; Karki, P.; Loh, Y. L.; Çakır, D. Strain−Spintronics: Modulating Electronic and Magnetic Properties of Hf2MnC2O2 MXene by Uniaxial Strain. *J. Phys. Chem. C* **2019**, *123*, 12451−12459.
(84) Cui, J.; Peng, Q.; Zhou, J.; Sun, Z. Strain-Tunable Electronic Structures and Optical Properties of Semiconducting MXenes. *Nanotechnology* **2019**, *30*, No. 345205.
(85) Johari, P.; Shenoy, V. B. Tuning the Electronic Properties of Semiconducting Transition Metal Dichalcogenides by Applying Mechanical Strains. *ACS Nano* **2012**, *6*, 5449−5456.
(86) Albright, T. A. B.; Jeremy, K.; Whangbo, M. H. *Orbital Interactions in Chemistry*; John Wiley & Sons, Inc.: New York, 1985.
(87) Hoffmann, R. Interaction of Orbitals through Space and through Bonds. *Acc. Chem. Res.* **1971**, *4*, 1−9.
(88) Peng, X.; Copple, A. Origination of the Direct-Indirect Band gap Transition in Strained Wurtzite and Zinc-blende GaAs Nanowires: A First Principles Study. *Phys. Rev. B* **2013**, *87*, No. 115308.
(89) Wu, Y. T.; Nie, P.; Wu, L. Y.; Dou, H.; Zhang, X. G. 2D MXene/SnS2 Composites as High-Performance Anodes for Sodium Ion Batteries. *Chem. Eng. J.* **2018**, *334*, 932−938.
(90) Olson, C. L.; Nelson, J.; Islam, M. S. Defect Chemistry, Surface Structures, and Lithium Insertion in Anatase TiO2. *J. Phys. Chem. B* **2006**, *110*, 9995−10001.
(91) Lunell, S.; Stashans, A.; Ojamae, L.; Lindstrom, H.; Hagfeldt, A. Li and Na Diffusion in TiO2 from Quantum Chemical Theory versus Electrochemical Experiment. *J. Am. Chem. Soc.* **1997**, *119*, 7374−7380.
(92) Uthaisar, C.; Barone, V. Edge Effects on the Characteristics of Li Diffusion in Graphene. *Nano Lett.* **2010**, *10*, 2838−2842.
(93) Li, W.; Yang, Y.; Zhang, G.; Zhang, Y. W. Ultrafast and Directional Diffusion of Lithium in Phosphorene for High-Performance Lithium-Ion Battery. *Nano Lett.* **2015**, *15*, 1691−1697.
(94) Jing, Y.; Zhou, Z.; Cabrera, C. R.; Chen, Z. Metallic VS2 Monolayer: A Promising 2D Anode Material for Lithium Ion Batteries. *J. Phys. Chem. C* **2013**, *117*, 25409−25413.

https://dx.doi.org/10.1021/acs.chemmater.0c02139
Chem. Mater. 2020, 32, 6947−6957